SDS Adsorptions Films at the H_2O-Au(111) Interface: Molecular Dynamics Study of AFM Tip–Surface Contact

J. Hörmann, L. Pastewka

SDS Adsorptions Films at the $H_2O-Au(111)$ Interface: Molecular Dynamics Study of AFM Tip–Surface Contact

Johannes Hörmann and Lars Pastewka

Department of Microsystems Engineering, University of Freiburg,
Georges-Köhler-Allee 103, 79110 Freiburg, Germany
E-mail: lars.pastewka@imtek.uni-freiburg.de

On the example of the anionic model surfactant sodium dodecyl sulphate at the idealised water-gold interface, our present molecular dynamics simulations illuminate the interdependence of adsorption film morphology and its mechanical properties at the nanoscale. Distinct film phases exhibit unique force response features in modelled atomic force microscopy experiments.

1 Introduction

In aqueous solution, amphiphilic surfactants adsorb on immersed surfaces. Dependent on the specific molecule and concentration, they form surface structures of varying morphology: monolayers of flat-lying molecules, hemicylindrical stripes or full cylinders have all been observed. These films exhibit morphology-dependent mechanical properties, such as nanoscopic response under the atomic force microscope (AFM)[1] as well as macroscopic lubrication performance.[2] Our work focuses on the model surfactant sodium dodecyl sulphate (SDS) at the $H_2O-Au(111)$ interface, known to form flat-lying monolayers at low concentrations and stripe-like hemicylindrical aggregates with increasing adsorption mass.[3] This phase transition alters the boundary film's mechanical properties, and it was hypothesised that this facilitates stick-slip response[4] under frictional loading. We use an existing SDS parametrisation to simulate AFM experiments by means of classical all-atom molecular dynamics (MD), as illustrated in Fig. 1. Systematic exploration of the parametric space spanned by concentration, film morphology, as well as AFM probe approach velocity reveals distinctive behaviour along each of these dimensions.

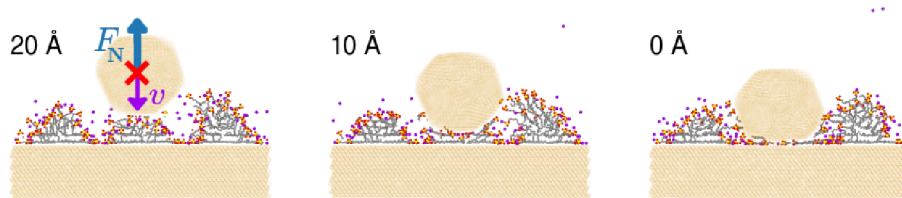Figure 1. $v = 1$ m s^{-1} approach of model AFM probe towards hemicylindrical SDS aggregates on Au(111). A purple velocity vector v implies the probe's linear approach, while a blue force vector F_N illustrates the film's resistance felt by the probe. Snapshot labels indicate surface–surface distance between probe and substrate.

2   Methods

We carry out classical MD simulations employing a valence force-field that allows modelling of physisorption processes but does not include breaking of covalent bonds. Parameters are taken from CHARMM[5] 36 and the INTERFACE force-field.[6] CHARMM has been reported to reproduce micellar properties of SDS well.[7] The rigid water model TIP3P (CHARMM standard) constitutes our explicit solvent. An embedded atom method potential by Grochola[8] describes the Au-Au interaction. A cubic Au block with one of its {111} surfaces exposed to the solution containing the SDS serves as substrate. It is sized as to accommodate three hemicylindrical surfactant aggregates of ~ 2.5 nm experimentally determined radius[9] on its surface. Sampling the full adsorption process from solution lies out of reach within the timescales accessible by brute-force MD. Hence, we preassemble a set of monolayers and hemicylinders at appropriate surface concentrations covering the adsorption isotherm's region of film phase transition. After minimisation, NVT-, and NPT-equilibration, all systems evolve for 10 ns, with only the substrate Langevin-tempered while pressurising the solution along the surface normal.

AFM probe models are prepared by melting gold spheres of 2.5 nm initial radius and subsequent slow quenching from 1800 K down to 298 K over a time span of 100 ns at 5 fs time step. Insertion at surface–surface distance $d = 3$ nm – sufficiently far as not to disturb the adsorption film structure – follows the parallel alignment of a probe's {111} facet with the substrate's (111) surface. Note that all surface–surface distances are stated with respect to perfect overlap of substrate's and probe's outermost atomic layer as zero reference. Succeeding repeated minimisation, NVT- and NPT-equilibration, substrate and probe are tempered by a dissipative particle dynamics (DPD) thermostat[10, 11] while holding the system volume fixed. After 0.5 ns, the probe model's frozen core of 2.4 nm diameter is instantaneously set into motion at prescribed velocity, approaching the substrate with its bottommost 1.4 nm layer immobile.

All calculations at the interface apply a 2 fs time step, 3D-periodic boundary conditions, and particle-particle particle-mesh Ewald summation treatment of long interactions. In the above, standard conditions of temperature $T = 298$ K and pressure $P = 1013$ hPa hold wherever applicable.

3   Results & Discussion

Estimating the drag force of our model AFM probe in water at standard conditions by means of Stokes' law for a bead in viscous fluid, $F_d = 6\pi\eta r v$, with probe radius

Stokes drag of the AFM probe			
velocity v [m s^{-1}]	10	1	0.1
analytical estimate F_d [nN]	0.15	0.02	~ 0
MD average F_d [nN]	1.27	0.15	0.02

Table 1. Viscous drag in TIP3P water as estimated for a bead of $r = 2.5$ nm by Stokes' law and as recorded via MD for our AFM tip model in bulk solution.

$r = 2.5$ nm and dynamic viscosity of the TIP3P rigid water model,[12] $\eta = 0.321$ mPa s, yields non-negligible drag for $v = 10$ m s^{-1} compared to the expected magnitude of adsorption film response. Tab. 1 shows estimated and measured viscous drag at slower speeds to diminish in comparison to the encountered film resistance. Viscous drag was measured as the average force acting on the probe for distances $d > 2.3$ nm above the substrate. Deviations from Stokes estimate are likely due to hydrodynamic interactions between tip and surface at the distances probed here.

Characteristic force response features are unidentifiable in the fast approach case of 10 m s^{-1}, as apparent in Fig. 2. Even the two slower approaches still exhibit non-negligible quantitative discrepancies. Yet, the two slowest approaches produce comparable qualitative features. From inset A of Fig. 2 (distance $d \sim 17$ Å) to Fig. 2B ($d \sim 13$ Å), the slightly compressed monolayer begins to reorder laterally under applied load. This is accompanied by a repulsive force on the indenter. For the slowest approach rate (0.1 m s^{-1}), there is a slight increase in force between snapshots A and B that we attribute to the initial triggering of the lateral tilt of the molecules. From Fig. 2C ($d \sim 11$ Å) to D ($d \sim 9$ Å), a forcefully
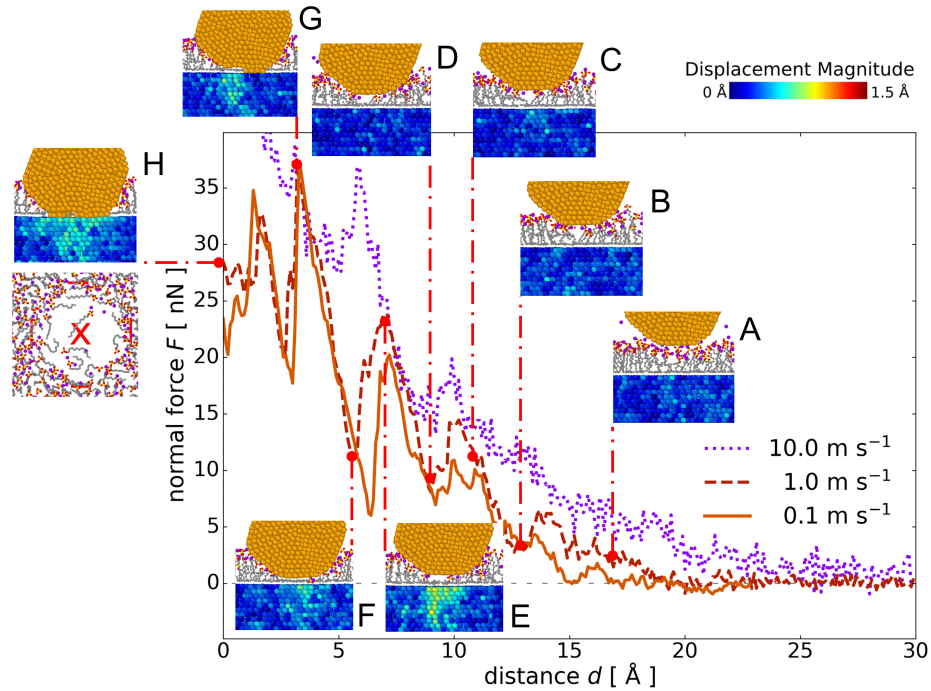

Figure 2. Velocity dependency of AFM force response. Figure shows normal force F on the AFM tip as a function of tip–surface distance d. Values at large d correspond to Stokes drag on the AFM tip reported in Tab. 1. The colour-coding of substrate atoms in the insets shows the displacement of each atom from its initial position for this particular snapshot. Varying substrate colouring for insets at $d \geq 10$ Å (A-D) reflects thermal fluctuations. Slight substrate deformation is evident for $d < 10$ Å (E-H). Panel H shows a top-view of only the SDS molecules in the contact area.

restructured film pushes the surfactant's hydrocarbon tails towards the surface, where they partially adhere to the substrate. This is accompanied by a slight drop in the repulsive force on the tip. At Fig. 2E ($d \sim 7$ Å), the head groups of molecules remaining within the gap protrude above a monomolecular hydrocarbon layer. Strong repulsion arises from the resistance against becoming a fully flat-lying monolayer, which needs to be accompanied by the movement of molecules out of the contact.

The colour-coded magnitude of substrate atom displacement (measured with respect initial position) reveals an indentation of the substrate clearly distinguishable from thermal fluctuations at this distance. While the colours in panels A-D are purely due to thermal fluctuations, panels E-H (forces $\gtrsim 10$nN) reveal and extended region of finite displacement that is due to the elastic deformation of the substrate. This means the surface does not feel a significant force from the indenter during initial approach A-D, as the whole deformation is localised within the thin adsorption film.

At Fig. 2F ($d \sim 5.5$ Å), only a monomolecular layer remains between tip and substrate. The stark drop in repulsive force is due to the onset of Au-Au interaction. Note that the employed EAM potential[8] has a cutoff radius of 5.5 Å, corresponding roughly to the position of the minimum in repulsive force marked by panel F. Events at closer distances, Fig. 2G to H, correspond to the probe's deformation around a few surfactant molecules trapped within the contact area, visualised in the contact area's top view of Fig. 2H at $d = 0$. It is remarkable that most surfactant molecules have been "squeezed out" of the contact. We believe that at even slower approach rates the remaining molecules should also be able to leave the contact by surface diffusion. Compromising between computational costs and accuracy, we use $1 \, \text{ms}^{-1}$ as reference velocity for the simulations described in the following.

Fig. 3 shows the variation of force–distance curves with surface concentration during approach of the AFM tip for homogeneous films. With increasing surface number
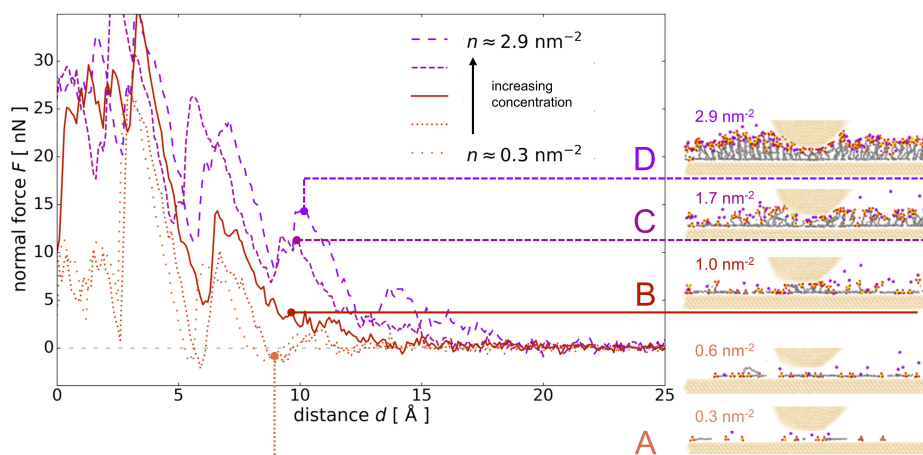

Figure 3. Distinguished AFM response features of SDS monolayers for increasing concentrations at $1 \, \text{m s}^{-1}$ approach velocity. Insets show snapshots around surface–surface distance $d \sim 10$ Å. At surface number concentrations as high as $2.9 \, \text{nm}^{-2}$, the morphology probed here does not constitute a realistic system anymore: The monolayer will have undergone a phase transition to hemicylindrical aggregates, as discussed below in Fig. 4.

concentration n, the simulated AFM force–distance curves exhibit transitions in characteristic features. In Fig. 3, the onset of a repulsive force felt by the approaching tip moves from below 15 Å at $n < 1\,\mathrm{nm}^{-2}$ towards 20 Å with increasing concentration up to $n \sim 2.9\,\mathrm{nm}^{-2}$. Highlighting only the most apparent distinction between the different concentrations probed here, we attribute the attractive contribution for low coverage $n < 1\,\mathrm{nm}^{-2}$ (Fig. 3A) between surface–surface distances of 8 to 10 Å to the hydrophobic interaction between bare hydrocarbon tails lying flat at the substrate surface and the approaching probe model. Note the absence of any interaction between the tip's and the surface's gold atoms at this distance. At $n \sim 1\,\mathrm{nm}^{-2}$ (Fig. 3B), the surface is homogeneously covered with surfactants and some head groups protrude into solution. The tip has just made contact with the adsorption film and the attractive contribution at this position has vanished. For even higher concentrations $n > 1\,\mathrm{nm}^{-2}$ (Fig. 3C and D), the probe compresses a densely packed film and forces surfactant molecules to tilt, thereby requiring a rearrangement of their environment. Because of this, the feature that was attractive at low concentrations is repulsive at high concentrations.

In experiments, homogeneous monolayers such as shown in Fig. 3D are not observed at surface concentrations as high as $2.9\,\mathrm{nm}^{-2}$. Instead, the film will have completed its phase transition to hemicylindrical aggregates. Within the timescales probed in these calculations, both phases are (meta)stable when evolving from artificially preassembled initial configurations. Fig. 4 contrasts probing of these different morphologies under otherwise equivalent conditions, in particular under equal surface concentration. The curves exhibit distinct behaviour within the $d \in [10, 15]$ Å region. Cross-sectional views (Fig. 4 A1, B1)
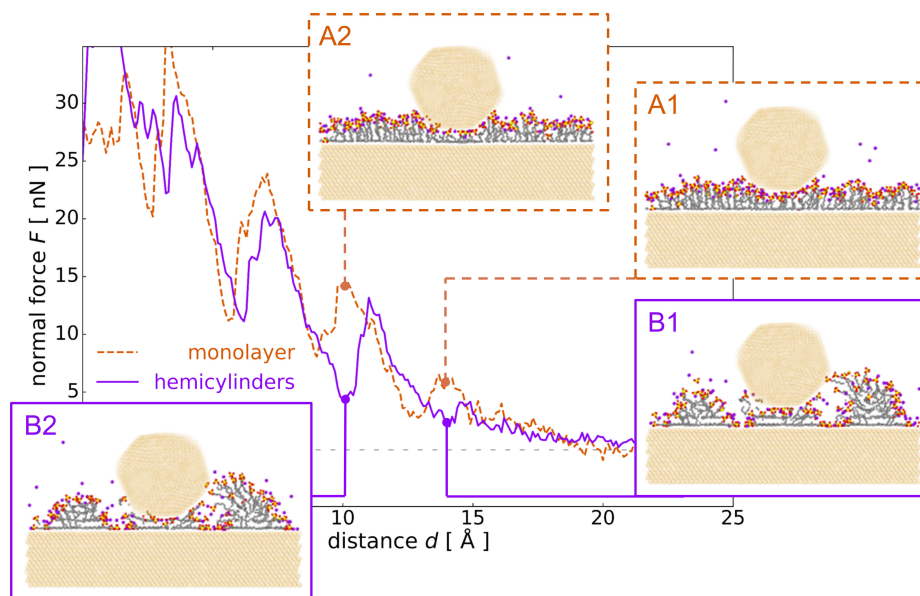

Figure 4. $1\,\mathrm{m\,s}^{-1}$ AFM probe approach above hypothetical monolayer and experimentally observed hemicylindrical aggregates of SDS at $2.9\,\mathrm{nm}^{-2}$. Insets show snapshot cross sections at gap widths $d \sim 14$ Å and $d \sim 10$ Å.

at $d \sim 14$ Å and (Fig. 4 A2, B2) at $d \sim 10$ Å reveal different ordering of the surfactant molecules that remain in the narrow gap between tip and surface: While surfactant molecules strive to stand upright on the surface within the artificially dense monolayer (Fig. 4 A1, A2), hemicylindrical configurations accommodate molecules that are aligned parallel to the surface (Fig. 4 B1, B2). Only head groups are in contact with the tip in the dense monolayer case. Contrastingly, the indented hemicylindrical aggregate allows tangentially aligned hydrocarbon tails to wet the probe surface at $d \sim 10$ Å (Fig. 4 B2). Constituents of neighbouring aggregates stretch to adhere to the unpassivated probe with their head groups in the case of striped aggregates (Fig. 4 B1, B2). The resulting force–distance curves have qualitatively different features, in particular a peak in the repulsive force at $d \sim 14$ Å for the monolayer (Fig. 4 A1) that is absent for the striped aggregates (Fig. 4 B1).

4   Summary & Conclusions

For the example of the anionic surfactant SDS, we have shown that MD-simulated AFM force–distance curves exhibit morphology-dependent characteristics. We systematically explored the impact of probe velocity and surfactant concentration on measured normal forces, showing that with changing surfactant concentration we expect qualitative changes in the force–distance curves. Subsequently, comparison between the experimentally observed hemicylindrical aggregates and purely hypothetical monolayers at high surface concentrations revealed distinct force response features. Thus, we have highlighted the impact of three different parametric dimensions, namely probe velocity, surfactant concentration, and film morphology on the manifestation of force–distance curves in MD simulations of AFM experiments. These calculations demonstrate MD to be a promising tool in understanding the nanoscopic mechanisms behind mechanical properties of surfactant adsorption films.

Acknowledgements

References

1. I. Burgess, C. A. Jeffrey, X. Cai, G. Szymanski, Z. Galus, and J. Lipkowski, *Direct Visualization of the Potential-Controlled Transformation of Hemimicellar Aggregates of Dodecyl Sulfate into a Condensed Monolayer at the Au(111) Electrode Surface*, Langmuir **15**, 2607–2616, 1999.

2. J. Zhang and Y. Meng, *Boundary Lubrication by Adsorption Film*, Friction **3**, 115–147, 2015.

3. M. Chen, I. Burgess, and J. Lipkowski, *Potential Controlled Surface Aggregation of Surfactants at Electrode Surfaces - A Molecular View*, Surf. Sci. **603**, 1878–1891, 2009.

4. J. Zhang and Y. Meng, *Stick–Slip Friction of Stainless Steel in Sodium Dodecyl Sulfate Aqueous Solution in the Boundary Lubrication Regime*, Tribol. Lett. **56**, 543–552, 2014.

5. R. B. Best, X. Zhu, J. Shim, P. E. M. Lopes, J. Mittal, M. Feig, and A. D. MacKerell, *Optimization of the Additive CHARMM All-Atom Protein Force Field Targeting Improved Sampling of the Backbone ϕ, ψ and Side-Chain X_1 and X_2 Dihedral Angles*, J. Chem. Theory Comput. **8**, 3257–3273, 2012.

6. H. Heinz, T. J. Lin, R. Kishore Mishra, and F. S. Emami, *Thermodynamically Consistent Force Fields for the Assembly of Inorganic, Organic, and Biological Nanostructures: The INTERFACE Force Field*, Langmuir **29**, 1754–1765, 2013.

7. X. Tang, P. H. Koenig, and R. G. Larson, *Molecular Dynamics Simulations of Sodium Dodecyl Sulfate Micelles in Water – The Effect of the Force Field*, J. Phys. Chem. B **118**, 3864–3880, 2014.

8. G. Grochola, S. P. Russo, and I. K. Snook, *On Fitting a Gold Embedded Atom Method Potential Using the Force Matching Method*, J. Chem. Phys. **123**, 204719, 2005.

9. M. Jaschke, H. Butt, H. E. Gaub, and S. Manne, *Surfactant Aggregates at a Metal Surface*, Langmuir **13**, 1381–1384, 1997.

10. R. D. Groot and P. B. Warren, *Dissipative Particle Dynamics: Bridging the Gap between Atomistic and Mesoscopic Simulation*, J. Chem. Phys. **107**, 4423–4435, 1997.

11. T. Soddemann, B. Dünweg, and K. Kremer, *Dissipative Particle Dynamics: A Useful Thermostat for Equilibrium and Nonequilibrium Molecular Dynamics Simulations*, Phys. Rev. E **68**, 46702, 2003.

12. M. A. González and J. L. F. Abascal, *The Shear Viscosity of Rigid Water Models*, J. Chem. Phys. **132**, 096101, 2010.

13. S. Plimpton, *Fast Parallel Algorithms for Short-Range Molecular Dynamics*, J. Comput. Phys. **117**, 1–19, 1995.

14. A. Stukowski, *Visualization and Analysis of Atomistic Simulation Data with OVITO–the Open Visualization Tool*, Model. Simul. Mater. Sc. **18**, 015012, 2009.

15. W. Humphrey, A. Dalke, and K. Schulten, *VMD: Visual Molecular Dynamics*, J. Mol. Graphics **14**, 33–38, 1996.

16. L. Martinez, R. Andrade, E. G. Birgin, and J. M. Martínez, *PACKMOL: A Package for Building Initial Configurations for Molecular Dynamics Simulations*, J. Comput. Chem. **30**, 2157–2164, 2009.

17. A. Jain, S. P. Ong, W. Chen, B. Medasani, X. Qu, M. Kocher, M. Brafman, G. Petretto, G. M. Rignanese, G. Hautier, D. Gunter, and K. A. Persson, *FireWorks: a dynamic workflow system designed for highthroughput applications*, Concurrency Computat.: Pract. Exper. **27**, 5037–5059, 2015.